La_2NiSb – A Ternary Ordered Version of the Bi_3Ni Type with Highly Polar Bonding

Konrad Schäfer[a], Anna Isaeva[b], Michael Ruck[b,c], Birgit Gerke[a], Christian Schwickert[a], and Rainer Pöttgen[a]

[a] Institut für Anorganische und Analytische Chemie, Universität Münster, Corrensstrasse 30, 48149 Münster, Germany

[b] Fachrichtung Chemie und Lebensmittelchemie, Technische Universität Dresden, Helmholtzstrasse 10, 01069 Dresden, Germany

[c] Max-Planck-Institut für Chemische Physik fester Stoffe, Nöthnitzer Straße 40, 01187 Dresden, Germany

Reprint requests to R. Pöttgen. E-mail: pottgen@uni-muenster.de

Z. Naturforsch. **2014**, *69b*, 1097 – 1104 / DOI: 10.5560/ZNB.2014-4135
Received June 27, 2014

Dedicated to Professor Hubert Schmidbaur on the occasion of his 80th birthday

The lanthanum-rich antimonide La_2NiSb was synthesized by annealing a cold-pressed pellet of the elements in a sealed silica glas tube at 1120 K. La_2NiSb was characterized by powder and single-crystal X-ray diffraction: ordered Bi_3Ni type, *Pnma*, $Z = 4$, $a = 825.6(3)$, $b = 452.2(2)$, $c = 1195.5(4)$ pm, $wR = 0.0695$, 856 F^2 values, 26 variables. The nickel atoms form infinite zigzag chains (259 pm Ni–Ni) with trigonal-prismatic lanthanum coordination for each nickel atom. The antimony atoms cap the rectangular faces of the lanthanum prisms (336 pm La–Sb) and thereby coordinate also the nickel atoms (271 pm Ni–Sb). These rods run parallel to the *b* axis and form a herringbone pattern, similar to the FeB-type structure of GdNi. Although metallic conductivity is expected for La_2NiSb from DFT-based band structure calculations, the real-space bonding analysis shows prominent localization of electrons on antimonide anions and positively charged lanthanum cations. The chain substructure is strongly bonded by polar covalent Ni–Sb and multicenter Ni–Ni interactions. The nickel atoms, which are involved in multicenter bonding with adjacent nickel and lanthanum atoms, provide a conductivity pathway along the prismatic strands. ^{121}Sb Mössbauer spectroscopic data at 78 K show a single signal at an isomer shift of $-7.62(3)$ mm s^{-1}, supporting the antimonide character. La_2NiSb shows weak paramagnetism with a susceptibility of 2.5×10^{-3} emu mol^{-1} at room temperature.

Key words: Lanthanum, Antimonide, Metal-rich Compound, Crystal Structure, Chemical Bonding

Introduction

The rare earth (*RE*) metals react with a transition metal (*T*) and antimony, forming a huge variety of ternary antimonides with broadly varying crystal-chemical features. The many crystallographic data have been summarized in a review by Sologub and Salamakha [1]. Among these compounds, the equiatomic phases *RET*Sb have been most intensively investigated, especially the cerium-, europium-, and ytterbium-containing ones, because they are potential candidates for valence instabilities. The basic data for these antimonides have been reviewed [2 – 8]. Another very interesting series concerns the skutterudites RET_4Sb_{12} which have been thoroughly studied in the context of thermoelectric materials [9].

Most of the $RE_xT_ySb_z$ phases have comparatively high antimony contents, leading to pronounced antimony substructures. Only a few rare earth-rich phases are known, especially the Mo_5B_2Si-type antimonides RE_5T_2Sb [10 – 12] which contain isolated antimony atoms (*i. e.* no Sb–Sb bonding) in square-antiprismatic rare earth coordination. In continuation of our systematic studies of hydrogenation experiments of the equiatomic La*T*Sb and Ce*T*Sb antimonides [6] we obtained the new lanthanum-rich antimonide La_2NiSb. The targeted synthesis, crystal chemistry, chemical bonding, and properties are reported herein. The pe-

culiar topic of this contribution concerns the crystal-chemical relation of La_2NiSb with the bulk superconductor Bi_3Ni [13 – 16].

Experimental

Synthesis

Starting materials for the synthesis of polycrystalline samples of La_2NiSb were lanthanum ingots (Smart elements), nickel powder (Merck) and antimony shots (Johnson Matthey), all with stated purities higher than 99 %. Filings of lanthanum were prepared under paraffin oil, washed with cyclohexane (both dried over sodium wire) and kept in Schlenk tubes prior to the reactions. The elements were mixed in a mortar, subsequently cold-pressed to pellets of 6 mm diameter and sealed in evacuated silica glas tubes. The ampoules were heated in muffle furnaces up to 1120 K within 96 h and kept at that temperature for 500 h. The samples were cooled down to room temperature over a period of 96 h. The resulting powders were dark grey. They are stable in air for a few days before starting slow hydrolysis.

Below a reaction temperature of 920 K no reaction to La_2NiSb was observed. At temperatures above 1170 K an anti-Th_3P_4-type phase with an approximate composition $La_4Ni_{1.5}Sb_{1.5}$ could be obtained. The refined lattice parameter of this cubic decomposition product was 964.65(6) pm. This phase can also be obtained by melting polycrystalline La_2NiSb.

EDX data

Semiquantitative EDX analyses of the crystal investigated on the diffractometer was carried out by use of a Zeiss EVO® MA10 scanning electron microscope in variable pressure mode with LaF_3, nickel and antimony as standards. The experimentally observed composition (52 ± 3 at.-% La; 28 ± 3 at.-% Ni; 20 ± 3 at.-% Sb) was close to the calculated one. No impurity elements heavier than sodium (detection limit of the instrument) were observed.

X-Ray diffraction

The polycrystalline La_2NiSb samples were characterized by Guinier powder diffractometry ($CuK_{\alpha 1}$ radiation, internal α-quartz standard: $a = 491.30$ pm, $c = 540.46$ pm). The Guinier camera was equipped with an imaging plate technique (Fujifilm, BAS-1800). The orthorhombic lattice parameters (Table 1) were obtained from a least-squares refinement. Correct indexing was ensured by an intensity calculation [17].

Small crystalline fragments were selected from the La_2NiSb samples. The suitability for intensity data collection was first checked by Laue photographs on a Buerger camera (white Mo radiation). A data set of a good-quality crystal was collected at room temperature using a Stoe IPDS-II image plate system (graphite-monochromatized MoK_α radiation; $\lambda = 71.073$ pm) in oscillation mode. A numerical absorption correction was applied to the data set. The relevant crystallographic data and details of the data collection and evaluation are listed in Table 1.

Table 1. Crystal data and structure refinement for La_2NiSb, space group *Pnma*, $Z = 4$.

Empirical formula	La_2NiSb
Diffractometer type	IPDS-II
Pearson symbol	oP16
Formula weight, g mol^{-1}	458.3
Unit cell dimensions (Guinier powder data)	
a, pm	825.6(3)
b, pm	452.2(2)
c, pm	1195.5(4)
Cell volume, nm^3	0.4463
Calculated density, g cm^{-3}	6.82
Crystal size, μm^3	$20 \times 30 \times 40$
Detector distance, mm	80
Exposure time, min	3
ω range; increment, deg	0 – 180; 1.0
Integr. param. (A / B / EMS)	14.0 / 3.7 / 0.013
Absorption coefficient, mm^{-1}	28.7
Transm. ratio (max/min)	1.57
$F(000)$, *e*	772
θ range for data collection, deg	3 – 32
Range in *hkl*	± 12, ± 6, ± 17
Total no. reflections	9263
Independent reflections / R_{int}	856 / 0.1932
Reflections with $I > 2\,\sigma(I)$ / R_σ	496 / 0.0844
Data/parameters	856 / 26
Goodness-of-fit on F^2	1.02
$R1$ / $wR2$ for $I > 2\,\sigma(I)$	0.0343 / 0.0629
$R1$ / $wR2$ for all data	0.0761 / 0.0695
Extinction coefficient	34(11)
Largest diff. peak / hole, *e* Å^{-3}	2.54 / −3.54

Structure refinement

Careful examination of the data set showed a primitive orthorhombic lattice, and the systematic extinctions were compatible with space group *Pnma*. The starting atomic parameters were deduced using the charge-flipping algorithm of SUPERFLIP [18], and the structure was refined with anisotropic displacement parameters for all atoms with JANA2006 [19]. The solution of the structure revealed the Pearson code *oP*16 with Wyckoff sequence c^4. Inspection of the Pearson data base [20] readily indicated isotypism with Bi_3Ni [13]. The La_2NiSb structure was then refined with the setting of the prototype. Separate refinement of the occupancy parameters revealed no deviations from the stoichiometric composition.

Table 2. Atomic coordinates, anisotropic and equivalent isotropic displacement parameters (pm^2) for La_2NiSb. All atoms lie on Wyckoff sites 4*c* (*x*, 1/4, *z*). The anisotropic displacement factor exponent takes the form: $-2\pi^2[(ha^*)^2U_{11}+\ldots+2hka^*b^*U_{12}]$. $U_{12}=U_{23}=0$. U_{eq} is defined as one third of the trace of the orthogonalized U_{ij} tensor. The positional parameters of the prototype Bi_3Ni [13] are listed for comparison in italics.

Atom	*x*	*z*	U_{11}	U_{22}	U_{33}	U_{13}	U_{eq}
La1	0.45894(11)	0.20437(7)	118(4)	172(5)	109(4)	−11(3)	133(2)
Bi1	*0.4114*	*0.17901*					
La2	0.21518(11)	0.95058(8)	120(4)	176(5)	123(4)	−12(3)	140(3)
Bi2	*0.2981*	*0.88968*					
Ni	0.0700(3)	0.52069(18)	167(10)	240(13)	200(10)	−59(8)	202(7)
Ni	*0.0897*	*0.5193*					
Sb	0.33012(12)	0.65852(9)	119(5)	166(6)	121(4)	−25(3)	136(3)
Bi3	*0.3820*	*0.59301*					

Table 3. Interatomic distances (pm) calculated with the powder lattice parameters of La_2NiSb. All distances within the first coordination spheres are listed. Standard deviations are all equal or less than 0.3 pm.

La1:	1	Ni	284.3	Ni:	2	Ni	258.7
	2	Ni	316.1		1	Sb	270.7
	2	Sb	329.1		1	La1	284.3
	2	Sb	333.3		1	La2	294.9
	1	La2	364.1		2	La2	299.3
	2	La2	397.3		2	La1	316.1
	2	La2	398.0	Sb:	1	Ni	270.7
La2:	1	Ni	294.9		2	La1	329.1
	2	Ni	299.3		2	La1	333.3
	2	Sb	338.1		2	La2	338.1
	1	Sb	343.6		1	La2	343.6
	1	Sb	361.8		1	La2	361.8
	1	La1	364.1				
	2	La1	397.3				
	2	La1	398.0				

The final difference Fourier synthesis revealed no significant residual peaks (Table 1). The atomic parameters and interatomic distances are listed in Tables 2 and 3.

Further details of the crystal structure investigation may be obtained from Fachinformationszentrum Karlsruhe, 76344 Eggenstein-Leopoldshafen, Germany (fax: +49-7247-808-666; e-mail: crysdata@fiz-karlsruhe.de, http://www.fiz-karlsruhe.de/request_for_deposited_data.html) on quoting the deposition number CSD-427930.

Mössbauer spectroscopy

A $Ba^{121m}SnO_3$ source was available for the Mössbauer spectroscopic measurement, which was conducted in the usual transmission geometry. The sample was enclosed in a small PMMA container at a thickness corresponding to about 10 mg Sb per cm^2. The measurement was performed in a commercial liquid nitrogen bath cryostat at 78 K. Fitting of the data was done by using the NORMOS-90 program package [21].

Magnetic susceptibility measurements

Susceptibility measurements of several La_2NiSb samples were carried out on a Quantum Design Physical Property Measurement System using the Vibrating Sample Magnetometer (VSM) option. For the measurements 10 – 20 mg of the powdered samples were packed in polypropylene capsules and attached to the sample holder rod. The measurements were performed in the temperature range of 2 – 305 K with magnetic flux densities up to 80 kOe ($1\ kOe = 7.96\times10^4\ A\ m^{-1}$).

Chemical bonding and band structure analyses

Scalar-relativistic DFT calculations were performed using the full-potential LAPW method [22] within the local-density approximation (LDA). Chemical bonding was characterized through the topological analysis of the electron localizability indicator (ELI-D, $\Upsilon^{\sigma}{}_{D}$) [23, 24] utilizing the DGRID program package [25] and using the PARAVIEW program package [26] for visualization. Formal atomic charges were calculated *via* integration of the electron density (ρ) in basins according to the quantum theory of atoms in molecules (QTAIM) developed by Bader [27]. The ELI-BON [28] values were computed from the ELI-D field employing similar partitioning and integration procedures.

Discussion

Crystal chemistry

The high-temperature reaction of the elements yielded a pure sample (according to powder X-ray diffraction, *vide infra*) of the new metal-rich antimonide La_2NiSb. The compound crystallizes with a ternary ordered version of the Bi_3Ni type [13], space group *Pnma*, and lattice parameters $a = 825.6(3)$, $b = 452.2(2)$, $c = 1195.5(4)$ pm. The La1, La2 and Sb atoms correspond to the Bi1, Bi2 and Bi3 sites, respectively, of the binary compound. Although the four

crystallographically independent atoms in both structures occupy similar Wyckoff sites 4*c*, substitution by different elements leads to drastic distortions. Besides the lattice parameters ($a = 887.96$, $b = 409.97$, $c = 1147.8$ pm for Bi_3Ni), also the positional parameters (Table 2) show substantial differences. Keeping these dissimilarities in mind (Figs. 1 and 2), one should call the structural relationship between Bi_3Ni and La_2NiSb isopointal [29, 30] rather than isotypic.

The near-neighbor coordination of the nickel and antimony atoms in La_2NiSb is presented in Fig. 1. The nickel atoms have slightly distorted trigonal-prismatic lanthanum coordination. The lanthanum prisms share rectangular faces to form a rod that runs parrallel to the *b* axis. Antimony atoms cap the outer rectangular faces of the lanthanum prisms (336 pm La–Sb) and thereby also coordinate the nickel atoms (271 pm Ni–Sb). The adjacent nickel atoms within the chain and the antimony atom amend the coordination of the nickel atom to a tricapped trigonal prism. Coordination number 9 for transition metals is frequently observed in related intermetallic structure types [31]. Within the chains the Ni–Ni distances of 259 pm are 10 pm longer than in *fcc* nickel [32]. Similar nickel chains (244 pm Ni–Ni) with end-on-coordinated cadmium atoms occur in the Mn_2B_2Al-type intermetallics RE_2Ni_2Cd [33, 34]. The nickel chain in binary Bi_3Ni is shown for comparison in Fig. 1. The Ni–Ni distances (263 pm) are slightly longer than in La_2NiSb; however, the striking difference concerns the Ni–Ni–Ni angle: 121.8° in La_2NiSb *vs.* 102.2° in Bi_3Ni.

The coordination of the antimony atoms in La_2NiSb is shown at the bottom of Fig. 1. Again we find coordination number 9 and a tricapped trigonal prism as coordination polyhedron. The Ni–Sb distance of 271 pm is significantly longer than the sum of the covalent radii for nickel and antimony of 256 pm [35]. Typically, the Ni–Sb distances within diverse polyanions are closer to the sum of the covalent radii, *e. g.* 258 to 267 pm in $PrNiSb_3$ [36] or 257 to 271 pm in Zr_3NiSb_7 [37].

The cutout of the La_2NiSb structure presented in Fig. 1 can be considered as fundamental building unit. The chains extend in *b* direction, and the adjacent chains are arranged in a herringbone pattern (Fig. 2). This motif can also be described as a strongly distorted hexagonal rod packing. The comparison with the fundamental units of Bi_3Ni readily shows that the tilt of the building units (realized by differences in the lattice parameters as well as by significant shifts in the atomic parameters) is much more pronounced in the La_2NiSb structure. The ionic character of the antimony and lanthanum atoms is mirrored in the orientations of the rods, which are somewhat different in La_2NiSb and Bi_3Ni. In the latter, the capping atom Bi3 has six neighbor atoms in adjacent rods. The average interrod distances (367 pm) are 20 pm longer than those to bismuth atoms within the rod, indicating comparatively weak bonding between the rods. In La_2NiSb, however, the capping antimony atom has only four lanthanum neighbors in adjacent rods, and the average Sb–La interrod distances (344 pm) are only 5 pm longer than the intrarod distances.

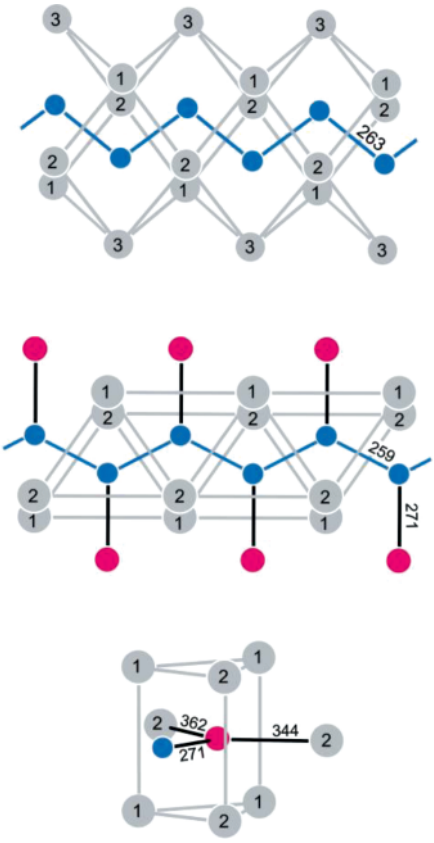

Fig. 1 (color online). (top and middle) Cut-outs of the Bi_3Ni and La_2NiSb structures. The zig-zag chains of the nickel atoms with trigonal prisms of lanthanum (bismuth) are emphasized. The antimony atoms coordinate end-on to each nickel atom. (bottom) Tricapped trigonal-prismatic coordination of the antimony atoms in La_2NiSb. Relevant interatomic distances (in pm) and the two crystallographically independent lanthanum (bismuth) sites are emphasized.

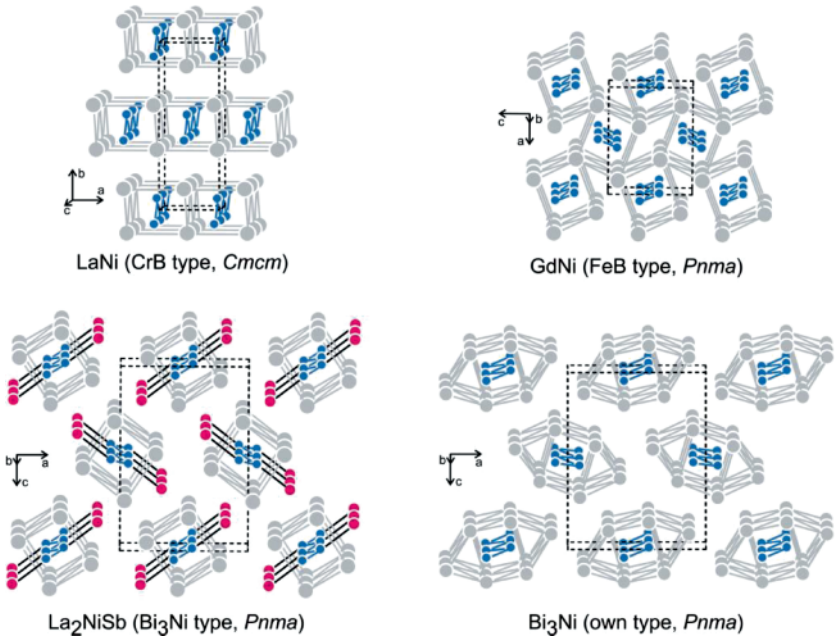

Fig. 2 (color online). The structures of LaNi, GdNi, La_2NiSb, and Bi_3Ni. Rare earth (bismuth), nickel and antimony atoms are drawn as light-grey, blue and red circles, respectively. The different rows of infinite nickel zig-zag chains in trigonal-prismatic rare earth (bismuth) coordination are emphasized.

The herringbone pattern arrangement of the zig-zag chains readily reminds the FeB-type structure [38]. For a binary nickel compound we present the GdNi structure [39] (drawn with the positional parameters of HoNi [40]) in Fig. 2. Also LaNi [41] (drawn with the positional parameters of CeNi [42]) contains infinite zig-zag chains, however, in another arrangement (CrB type). Starting from the FeB structure one needs to cut the common edges of the prismatic units, and the nickel chains are coordinated by the antimony atoms. Such cluster units also occur in various rare earth-rich compounds like Gd_4NiTe_2, $Er_5Ni_2Te_2$ or $Sc_5Ni_2Te_2$ [43] with similar ranges for the Ni–Ni distances.

Electronic structure and chemical bonding

Nickel-antimony chains clearly emerge as distinct strongly bonded building units in the course of the real-space bonding analysis. Two types of interactions form the one-dimensional strands: multicenter interactions that are predominantly contributed by two adjacent Ni atoms as well as, to a lesser extent, two overlying lanthanum atoms (ELI-D domains #1 in Fig. 3) and strongly polar covalent Ni–Sb bonds (ELI-D domains #2 in Fig. 3).

The latter disynaptic basin contains *ca.* 1.2 electrons, 56 % of which can be attributed to antimony *via* computation of the bond-polarity index [44]. Thus a covalent character of this bonding can be stated, although, as seen in Fig. 3c, the disynaptic basin is shifted towards the more electronegative atom and is significantly merged into the antimony valence shell.

The multisynaptic basins between the nickel atoms in the chain comprise about 0.5 electrons from each Ni constituent and about 0.14 electrons from each lanthanum, hence providing a one-dimensional conductivity pathway along the *b* axis. Furthermore, the nickel zig-zag entities also participate in the bonding with the outer prismatic lanthanum framework, as visualized by the ELI-D domains #3 in Fig. 3. The integration of the respective ELI-D basins yields four constituents: three lanthanum atoms from the triangular base of a prism, each contributing 0.2 electrons to the bonding, and one underlying nickel atom that brings in another 0.3 electrons. Apart from this, lanthanum is not involved in any bonding, and further topological analysis reveals monosynaptic basins. Less than 0.1 electron contributions can be found in the antimony valence shells from

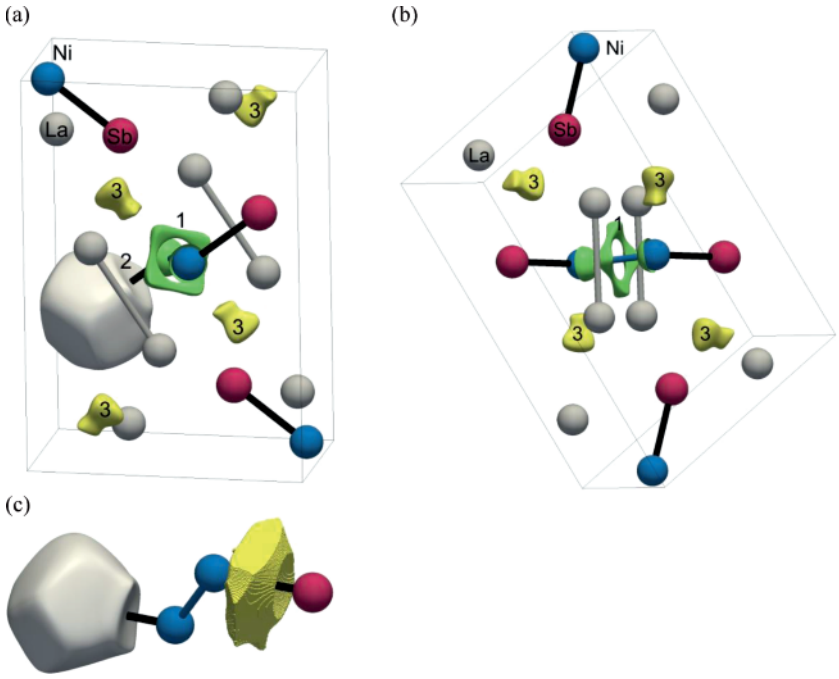

Fig. 3 (color online). A unit cell of La_2NiSb is outlined in (a) and (b). Grey circles depict lanthanum, blue are nickel, and magenta are antimony atoms. In (a) and (b) an isosurface ($\Upsilon = 0.75$) of a calculated ELI-D field is presented for selected localization domains: **1** – multicenter 2Ni–2La bonding; **2** – structured valence shell of antimony encompassing the Ni–Sb bonding; **3** – multicenter 3La–Ni interactions slightly off the trigonal base of a lanthanum prism. In (c) Ni–Sb bonding is presented in two ways: within an ELI-D localization domain (ELI isosurface) around Sb (grey; left) and as a distinct disynaptic basin found by partitioning of the ELI-D field (yellow; right).

neighboring "rods". Therefore mutual adjustment cannot be explained by bonding inter-rod interactions.

The band structure shows the borderline position of La_2NiSb between a metallic and an insulating state (Fig. 4). Given the metallic conductivity, a rod can be regarded as $[(La^{III})_2Ni^0(3e)]Sb^{-III}$ in a fully ionic scenario. The three "excess" electrons are responsible for the (strongly anisotropic) electrical conductivity. The reality is less extreme as supported by the Bader atomic charge analysis with charges of -1.4 for Sb, -0.84 for Ni and $+1.1$ for La. The calculated ELIBON values of -2.1 for Sb and $+3.1$ for La emphasize the isolated character of antimony anions and lanthanum cations more significantly. A sparse number of moderately dispersed bands, which are constituted mainly by nickel and antimony states, cross the Fermi level while forming a pseudo gap at the Γ point (Fig. 4). Thus the electrons are mostly localized, but an itinerant component is nevertheless present along the prismatic strands *via* Ni–Ni and Ni–La bonds.

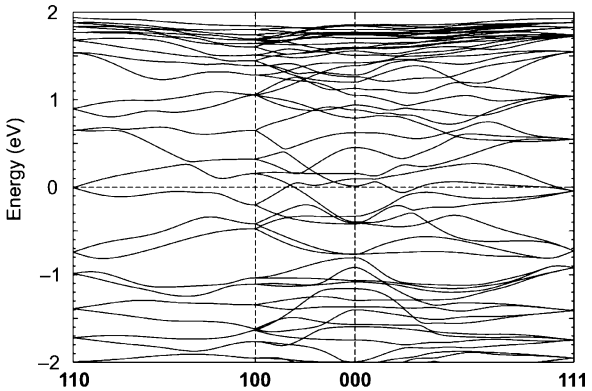

Fig. 4. Band structure for La_2NiSb; the Fermi level is set to 0 eV.

^{121}Sb Mössbauer spectroscopy

Fig. 5 shows the ^{121}Sb Mössbauer spectrum of La_2NiSb along with a transmission integral fit. The

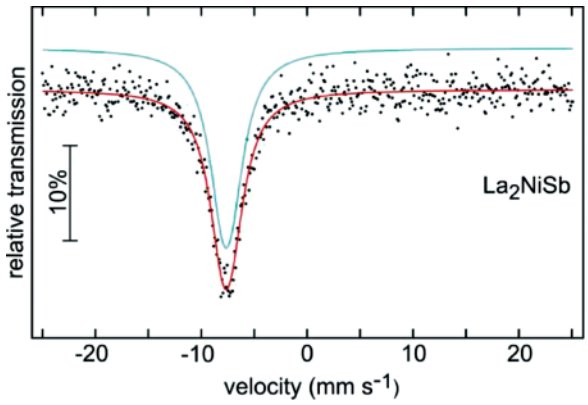

Fig. 5 (color online). Experimental (data points) and simulated (continuous line) ^{121}Sb Mössbauer spectrum of La_2NiSb at 78 K.

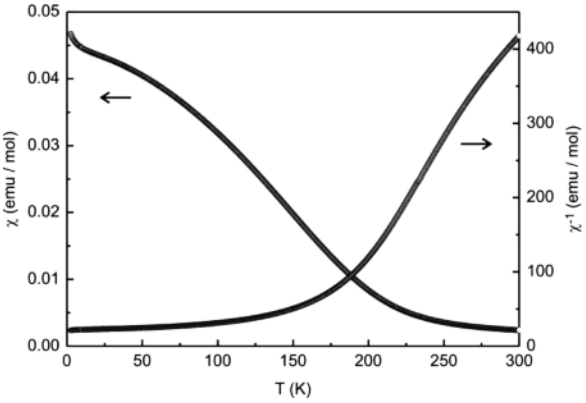

Fig. 6. Temperature dependence of the magnetic susceptibility (χ and χ^{-1} data) of La_2NiSb measured at 10 kOe.

spectrum was well reproduced by a single line at an isomer shift of $\delta = -7.62(3)\,\mathrm{mm\,s^{-1}}$. As a consequence of the low site symmetry of the antimony atoms, the signal is subjected to quadrupole splitting of $\Delta E_Q = 0.10(3)\,\mathrm{mm\,s^{-1}}$. The experimental line width of $\Gamma = 3.2(2)\,\mathrm{mm\,s^{-1}}$ is in the usual range. The isomer shift is close to the values observed for the series of Yb*T*Sb [4] and *RE*ZnSbO [45] compounds, or CeRhSb [6], nicely manifesting the antimonide character. A trivalent antimony cation would show a much more negative isomer shift, *e. g.* $-11.3\,\mathrm{mm\,s^{-1}}$ in Sb_2O_3 or $-14.5\,\mathrm{mm\,s^{-1}}$ for Sb_2S_3 [46].

Magnetic properties

The different La_2NiSb samples showed a weak susceptibility of 2.5×10^{-3} emu mol^{-1} at room temperature. The samples were all contaminated by very small amounts of an unknown ferromagnetic impurity (might be a consequence of the preparation technique), leading to an increase of the susceptibility between 300 and 150 K (Fig. 6). A field-dependent magnetization curve at 300 K showed linear increase as expected for a weakly paramagnetic material. At 150 K and 5 K the magnetization showed a spontaneous incease already at tiny fields as a consequence of the small ferromagnetic component. The almost saturation magnetization at 5 K and 80 kOe is 0.1 μ_B per formula unit (Fig. 7). Thus, keeping the small values in mind, La_2NiSb most likely behaves like a Pauli paramagnet. A similar behavior has been found for Bi_3Ni, which is essentially

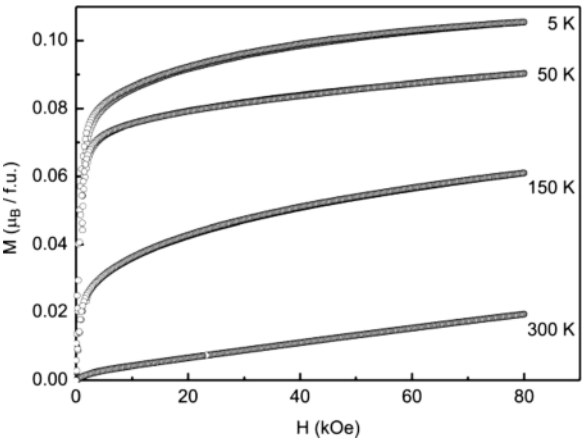

Fig. 7. Magnetization isotherms of the La_2NiSb sample at 5, 50, 150, and 300 K.

a Pauli paramagnet but shows ferromagnetic fluctuations on the surface [47]. In nano-structured samples of Bi_3Ni, this effect is much more pronounced due to the increased surface [14].

Acknowledgement

We thank Dipl.-Ing. U. Ch. Rodewald for the X-ray data collection. This work was financially supported by the Deutsche Forschungsgemeinschaft. We are indebted to the ZIH of TU Dresden for the computational facilities provided within the framework of the project "Chemical Bonding Analysis of Novel Inorganic Compounds with Real-Space Indicators".

[1] O. L. Sologub, P. S. Salamakha in *Handbook on the Physics and Chemistry of Rare Earths*, (Eds.: K. A. Gschneidner, Jr., J.-C. G. Bünzli, V. K. Pecharsky), Vol. 33, Elsevier Science B. V., Amsterdam, **2003**, chapter 212, pp. 35 – 146.

[2] R. Pöttgen, D. Johrendt, *Chem. Mater.* **2000**, *12*, 875.

[3] R. Pöttgen, D. Johrendt, D. Kußmann in *Handbook on the Physics and Chemistry of Rare Earths*, (Eds.: K. A. Gschneidner, Jr., L. Eyring, G. H. Lander), Vol. 32, North-Holland/Elsevier, Amsterdam, **2001**, chapter 207, pp. 453 – 513.

[4] R. Mishra, R. Pöttgen, R.-D. Hoffmann, Th. Fickenscher, M. Eschen, H. Trill, B. D. Mosel, *Z. Naturforsch.* **2002**, *57b*, 1215.

[5] A. Ślebarski, *J. Alloys Compd.* **2006**, *423*, 15.

[6] B. Chevalier, R. Decourt, B. Heying, F. M. Schappacher, U. Ch. Rodewald, R.-D. Hoffmann, R. Pöttgen, R. Eger, A. Simon, *Chem. Mater.* **2007**, *19*, 28.

[7] T. Mishra, I. Schellenberg, M. Eul, R. Pöttgen, *Z. Kristallogr.* **2011**, *226*, 590.

[8] J. Goraus, A. Ślebarski, *Phys. Status Solidi B* **2013**, *250*, 533.

[9] B. C. Sales in *Handbook on the Physics and Chemistry of Rare Earth*s, (Eds.: K. A. Gschneidner, Jr., J.-C. G. Bünzli, V. K. Pecharsky), Vol. 33, Elsevier Science B. V., Amsterdam, **2003**, chapter 211, pp. 1 – 34.

[10] Y. Mozharivskyj, Yu. B. Kuz'ma, *J. Alloys Compd.* **1996**, *236*, 203.

[11] Y. Mozharivskyj, H. F. Franzen, *J. Solid State Chem.* **2000**, *152*, 478.

[12] Y. Mozharivskyj, H. F. Franzen, *J. Alloys Compd.* **2001**, *327*, 78.

[13] M. Ruck, T. Söhnel, *Z. Naturforsch.* **2006**, *61b*, 785.

[14] T. Herrmannsdörfer, R. Skrotzki, J. Wosnitza, D. Köhler, R. Boldt, M. Ruck, *Phys. Rev. B* **2011**, *83*, 140501.

[15] J. Kumar, A. Kumar, A. Vajpayee, B. Gahtori, D. Sharma, P. K. Ahluwalia, S. Auluck, V. P. S. Awana, *Supercond. Sci. Techn.* **2011**, *24*, 085002.

[16] R. Boldt, A. Grigas, M. Heise, T. Herrmannsdörfer, A. Isaeva, S. Kaskel, D. Köhler, M. Ruck, R. Skrotzki, J. Wosnitza, *Z. Anorg. Allg. Chem.* **2012**, *638*, 2035.

[17] K. Yvon, W. Jeitschko, E. Parthé, *J. Appl. Crystallogr.* **1977**, *10*, 73.

[18] L. Palatinus, G. Chapuis, *J. Appl. Crystallogr.* **2007**, *40*, 786.

[19] V. Petříček, M. Dušek, L. Palatinus, *Z. Kristallogr.* **2014**, *229*, 345.

[20] P. Villars, K. Cenzual, *Pearson's Crystal Data – Crystal Structure Database for Inorganic Compounds* (release 2013/14), ASM International, Materials Park, Ohio (USA) **2013**.

[21] R. A. Brand, NORMOS, Mössbauer Fitting Program, University of Duisburg, Duisburg (Germany) **2002**.

[22] The Elk FP-LAPW Code, **2009–2014**; http://elk.sourceforge.net.

[23] M. Kohout, *Faraday Discuss.* **2007**, *135*, 43.

[24] M. Kohout, *Int. J. Quantum Chem.* **2004**, *97*, 651.

[25] M. Kohout, DGRID (version 4.7), Radebeul (Germany) **2013**.

[26] PARAVIEW: Parallel visualization application, Sandia National Labs, Kitware Inc, Los Alamos National Labs **2008**; http://paraview.org.

[27] R. F. W. Bader, *Atoms in Molecules*, Oxford University Press, Oxford **1990**.

[28] I. Veremchuk, T. Mori, Yu. Prots, W. Schnelle, A. Leithe-Jasper, M. Kohout, Yu. Grin, *J. Solid State Chem.* **2008**, *181*, 1983.

[29] L. M. Gelato, E. Parthé, *J. Appl. Crystallogr.* **1987**, *20*, 139.

[30] E. Parthé, L. M. Gelato, *Acta Crystallogr.* **1984**, *A40*, 169.

[31] E. Parthé, L. Gelato, B. Chabot, M. Penzo, K. Cenzual, R. Gladyshevskii, *TYPIX–Standardized Data and Crystal Chemical Characterization of Inorganic Structure Types*, Gmelin Handbook of Inorganic and Organometallic Chemistry, 8th edition, Springer, Berlin **1993**.

[32] J. Donohue, *The Structures of the Elements,* Wiley, New York **1974**.

[33] F. Canepa, S. Cirafici, F. Merlo, M. Pani, C. Ferdeghini, *J. Magn. Magn. Mater.* **1999**, *195*, 646.

[34] Th. Fickenscher, U. Ch. Rodewald, D. Niepmann, R. Mishra, M. Eschen, R. Pöttgen, *Z. Naturforsch.* **2005**, *60b*, 271.

[35] J. Emsley, *The Elements*, Oxford University Press, Oxford **1999**.

[36] E. L. Thomas, R. T. Macaluso, H.-O. Lee, Z. Fisk, J. Y. Chan, *J. Solid State Chem.* **2004**, *177*, 4228.

[37] V. Romaka, A. Tkachuk, L. Romaka, *Acta Crystallogr.* **2008**, *E64*, i47.

[38] T. Bjurström, *Arkiv. Kemi Mineral. Geol.* **1933**, *11A*, 1.

[39] N. C. Baenziger, J. L. Moriarty, Jr., *Acta Crystallogr.* **1961**, *14*, 946.

[40] Y. Isikawa, K. Mori, K. Sato, M. Ohashi, Y. Yamaguchi, *J. Appl. Phys.* **1984**, *55*, 2031.

[41] A. E. Dwight, R. A. Conner, Jr., J. W. Downey, *Acta Crystallogr.* **1965**, *18*, 835.

[42] J. J. Finney, A. Rosenzweig, *Acta Crystallogr.* **1961**, *14*, 69.

[43] C. Magliocchi, F. Meng, T. Hughbanks, *J. Solid State Chem.* **2004**, *177*, 3896.

[44] S. Raub, G. Jansen, *Theor. Chem. Acc.* **2001**, *106*, 223.

[45] I. Schellenberg, T. Nilges, R. Pöttgen, *Z. Naturforsch.* **2008**, *63b*, 834.

[46] P. E. Lippens, *Solid State Commun.* **2000**, *113*, 399.

[47] X. Zhu, H. Lei, C. Petrovic, Y. Zhang, *Phys. Rev. B* **2012**, *86*, 024527.